



Probabilistic 4D blood flow tracking and uncertainty estimation

Ola Friman^{a,*}, Anja Hennemuth^a, Andreas Harloff^b, Jelena Bock^b, Michael Markl^{b,c}, Heinz-Otto Peitgen^a

^a Fraunhofer MEVIS, Bremen, Germany

^b University Hospital Freiburg, Freiburg, Germany

^c Northwestern University, Chicago, USA

ARTICLE INFO

Article history:

Available online 7 June 2011

Keywords:

Blood flow

Phase-Contrast MRI

Uncertainty

Sequential Monte Carlo

Probabilistic tracking

ABSTRACT

Phase-Contrast (PC) MRI utilizes signal phase shifts resulting from moving spins to measure tissue motion and blood flow. Time-resolved 4D vector fields representing the motion or flow can be derived from the acquired PC MRI images. In cardiovascular PC MRI applications, visualization techniques such as vector glyphs, streamlines, and particle traces are commonly employed for depicting the blood flow. Whereas these techniques indeed provide useful diagnostic information, uncertainty due to noise in the PC-MRI measurements is ignored, which may lend the results a false sense of precision. In this work, the statistical properties of PC MRI flow measurements are investigated and a probabilistic flow tracking method based on sequential Monte Carlo sampling is devised to calculate flow uncertainty maps. The theoretical derivations are validated using simulated data and a number of real PC MRI data sets of the aorta and carotid arteries are used to demonstrate the flow uncertainty mapping technique.

© 2011 Elsevier B.V. All rights reserved.

1. Introduction

Every measurement has an uncertainty associated with it. Knowing this uncertainty is paramount in science to assess the measurement and to accept or reject hypotheses based on it. In a decision making process, uncertainty causes risk; the higher the uncertainty the higher the risk of making a poor decision. In clinical situations, false decisions may have dramatic consequences, and it is therefore crucial to convey the uncertainty associated with medical measurements to make it possible to assess and control the risk. In this work, the uncertainty of Phase-Contrast (PC) MRI (Firmin et al., 1987; Nayler et al., 1986; Pelc et al., 1991b, 1994), an emerging clinical tool for quantifying tissue motion and blood flow, is addressed. PC MRI applies an encoding sequence that makes residual phase shifts of spins proportional to the velocity of their movement. Modern MRI scanners are able to acquire time-resolved PC measurements, resulting in 4D (3D + time) images in which each voxel contains a 3D motion or flow vector, see Fig. 1. A large range of clinical applications benefit from the information in such images. For example, information on the blood flow pattern may be used for assessing stenoses, aneurysms and heart valve function; to understand the development of vessel plaque; and to plan and follow-up surgical interventions in congenital heart disease (Harloff et al., 2009; Markl et al., 2007; Wigström et al., 1996).

* Corresponding author.

E-mail addresses: ola.friman@mevis.fraunhofer.de (O. Friman), anja.hennemuth@mevis.fraunhofer.de (A. Hennemuth), andreas.harloff@uniklinik-freiburg.de (A. Harloff), jelena.bock@uniklinik-freiburg.de (J. Bock), mmarkl@northwestern.edu (M. Markl), peitgen@mevis.fraunhofer.de (H.-O. Peitgen).

Traditional techniques for visualizing vector fields include vector glyphs, streamlines, pathlines and particle traces. Specifically, a pathline and a particle trace depict the trajectory of a zero-mass particle takes through a time-varying vector field $\mathbf{V}(\mathbf{x}) : \mathbb{R}^4 \rightarrow \mathbb{R}^3$, where \mathbf{x} denotes a 4-dimensional spatio-temporal position. In cardiovascular PC MRI applications, such visualization techniques are employed for visualizing blood flow patterns (Napel et al., 1992; Wigström et al., 1999). However, while a visualization of the flow pattern indeed provide useful diagnostic information, noise and uncertainty in the measurements are not conveyed, which may lead to a false sense of precision and misinterpretation of the data. In this work, uncertainty arising due to noise in the PC MRI images is investigated and visualized using the *distribution* of possible flow trajectories. Uncertainty in streamlines was briefly discussed by Napel et al. (1992) in one of the first papers on flow visualization, but the topic has since not been further developed. Instead, methods for exploring the uncertainty of streamline trajectories drawn in tensor fields in the context of Diffusion-Tensor MRI (DTI) have been reported in recent years (Behrens et al., 2003; Björnemo et al., 2002; Friman et al., 2006; Hagmann et al., 2003; Jones and Pierpaoli, 2005; Parker et al., 2003; Parker and Alexander, 2005). The common principle of these methods is to derive the local measurement uncertainty in each voxel and then propagate this uncertainty to the image level and visualize it using an uncertainty distribution or connectivity map. Following this approach, the statistical properties of PC MRI images are in this work first derived to describe the local uncertainty in the measured flow vectors. The distribution of the pathlines or particle traces drawn in the ensuing field of random vectors is then sampled and characterized using a

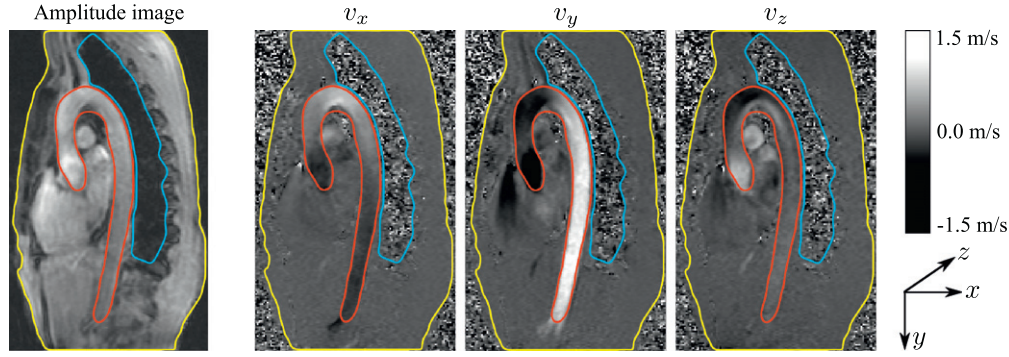


Fig. 1. One 2D slice of a Phase-Contrast MRI data set. The leftmost image shows the magnitude image $I(\mathbf{x})$, cf. Eq. (3). The three rightmost images show the flow velocities in the x , y , and z directions, estimated as described in Section 2.2. The body of the patient has been outlined in yellow, the aorta in red and the lung in blue. High flow can be seen in the aorta region. The probability distribution of the velocity components due to Gaussian image noise is shown to be Gaussian in the high-SNR areas. In the low-SNR areas outside the body and in the lung, the intensity distribution is different, which is clearly seen in the velocity images. (For interpretation of the references to colour in this figure legend, the reader is referred to the web version of this article.)

sequential Monte Carlo approach. A preliminary presentation of the work can be found in Friman et al. (2010).

2. Statistical properties of PC MRI flow vectors

In this section, the statistical distribution of the PC MRI flow vectors in the measured field $\mathbb{V}(\mathbf{x})$ in the presence of Gaussian thermal measurement noise is derived. The MRI noise affects the PC MRI images, and their statistical properties are therefore investigated first. Next, the distribution of an estimated flow vector $\hat{\mathbf{v}} \in \mathbb{V}$ is modeled, taking into account that modern MRI systems use phased-array coils consisting of a number of coils K , typically 4–16, to obtain better SNR and spatial coverage (Roemer et al., 1990). Finally a novel method for estimating unknown parameters such as the noise variance based on the acquired PC MRI images is introduced.

2.1. MRI magnitude and phase modeling

A complex MRI image in the spatial domain, i.e., after Fourier or k -space domain reconstruction, acquired with coil k in the phased-array may be modeled as

$$S_k(\mathbf{x}) = A_k(\mathbf{x})e^{i\theta_k(\mathbf{x})} + n_k^r + in_k^i, \quad (1)$$

where \mathbf{x} is a spatial voxel index, $A_k(\mathbf{x})$ represents the image magnitude weighted with the sensitivity of coil k , $\theta_k(\mathbf{x})$ is a coil-specific spatially varying phase, and n_k^r and n_k^i represent independent Gaussian noise $N(0, \sigma^2)$ in two quadrature channels (Conturo and Smith, 1990). From a statistical perspective, the magnitude $|S_k(\mathbf{x})|$ follows a Rician probability distribution (Macovski, 1996; Rice, 1944), which at high SNR ($A_k/\sigma > 5$) for all practical purposes can be approximated by a Gaussian distribution (Gudbjartsson and Patz, 1995):

$$|S_k(\mathbf{x})| \in N(A_k(\mathbf{x}), \sigma^2). \quad (2)$$

It should be mentioned that other approximations may be necessary at lower SNR (Andersen, 1996; Gudbjartsson and Patz, 1995; Henkelman, 1985; Koay and Basser, 2006), but the voxels of interest in PC MRI images, i.e., voxels containing tissue or blood, generally have a high Signal-to-Noise-Ratio (SNR). This will be further investigated in Section 5.

Without detailed knowledge of the of the spatial sensitivities of the coils, a near-optimal SNR magnitude image $I(\mathbf{x})$ with full spatial coverage is typically reconstructed from all coils using the sum-of-squares method (Roemer et al., 1990):

$$I(\mathbf{x}) = \sqrt{\sum_{k=1}^K |S_k(\mathbf{x})|^2}. \quad (3)$$

See Fig. 1 for an example image. The statistical properties of expressions as the one in Eq. (3) have been studied in Andersen and Kirsch (1996), and again, if the SNR is high for at least one coil, a Gaussian approximation can be applied

$$I(\mathbf{x}) \in N(A(\mathbf{x}), \sigma^2), \quad \text{with} \quad A(\mathbf{x}) = \sqrt{\sum_{k=1}^K A_k(\mathbf{x})^2}. \quad (4)$$

Note that $A(\mathbf{x})$ and σ^2 are unknown, but with the knowledge of the statistical distribution in Eq. (4), they can be estimated from the known $I(\mathbf{x})$. This estimation is described in Section 2.3.

The phase $\theta_k(\mathbf{x})$ in Eq. (1) is estimated with the argument operator $\arg(S_k(\mathbf{x}))$, and the exact probability distribution of this estimator is given in Gudbjartsson and Patz (1995). For high SNR, however, a simpler Gaussian approximation again provides an accurate approximation

$$\arg(S_k(\mathbf{x})) \in N_w\left(\theta_k(\mathbf{x}), \frac{\sigma^2}{A_k(\mathbf{x})^2}\right), \quad (5)$$

where N_w denotes a wrapped Normal distribution, i.e., θ_k is calculated modulo 2π so that $\theta_k \in (-\pi, \pi]$.

2.2. Flow velocity modeling

For a 3D PC velocity measurement, at least four separate images must be acquired and combined to obtain an estimated 3D flow vector $\hat{\mathbf{v}}(\mathbf{x})$ in every voxel, see the rightmost images in Fig. 1. A 4D flow field $\mathbb{V}(\mathbf{x}, t)$ is obtained by repeated acquisitions during the cardiac cycle synchronized with the RR-interval of the patient. There are different velocity encoding schemes which differ in the way the MRI gradient directions are applied (Conturo and Robinson, 1992; Pelc et al., 1991a). The unbalanced scheme is the most straightforward one, in which a baseline image S_k^0 and three images S_k^x , S_k^y , and S_k^z with additional velocity encodings along the x , y , and z directions are acquired (the spatial coordinate \mathbf{x} is dropped in this section for clarity as all calculations are carried out voxelwise), i.e., for each coil k , the following images are acquired, cf. Eq. (1):

$$\begin{cases} S_k^0 = A_k e^{i\theta_k} + \text{noise}, \\ S_k^x = A_k e^{i(\theta_k - \frac{\pi}{v_{enc}} v_x)} + \text{noise}, \\ S_k^y = A_k e^{i(\theta_k - \frac{\pi}{v_{enc}} v_y)} + \text{noise}, \\ S_k^z = A_k e^{i(\theta_k - \frac{\pi}{v_{enc}} v_z)} + \text{noise}. \end{cases} \quad (6)$$

In Eq. (6), v_x , v_y , and v_z are the flow velocities along the x , y , and z directions in every voxel, and the velocity encoding parameter v_{enc} is a known sequence parameter defining the range of velocities that can be measured. θ_k denotes an unknown and spatially varying phase term for coil k . As in Eq. (1), the noise is modeled as independent, complex and Gaussian. An image with the flow velocities is found by calculating the phase differences between the images in Eq. (6), i.e., if only on coil k is considered, v_x is estimated by

$$\tilde{v}_x = \frac{v_{enc}}{\pi} \arg \left(S_k^0 S_k^{*} \right), \quad (7)$$

where S_k^{*} denotes the complex conjugate of S_k . The v_y and v_z velocities are calculated analogously. Following the sum-of-squares reconstruction of the magnitude image in Eq. (3), a velocity estimate based on all K coils is as follows (Thunberg et al., 2005):

$$\tilde{v}_x = \frac{v_{enc}}{\pi} \arg \left(\sum_{k=1}^K S_k^0 S_k^{*} \right). \quad (8)$$

The estimator in Eq. (8) intrinsically weights the measurement in each coil k with the signal strength A_k^2 .

The goal in this section is to investigate the statistical properties of the velocity vectors estimated as described above. Again it should be emphasized that other encoding schemes are possible where other linear combinations of the v_x , v_y , and v_z velocities are acquired in Eq. (6), leading to slightly different reconstructions. The statistical derivations outlined below can be adapted to these alternative encodings with minor modifications. To derive the statistical distribution of the estimator in Eq. (8) under influence of the random noise, one may first observe that at high SNR, the following approximation can be made by omitting second-order terms that do not involve A_k (again focussing on v_x):

$$S_k^0 S_k^{*} \approx A_k^2 e^{i \frac{v_{enc}}{v_{enc}} v_x} + g_k^r + i g_k^i, \quad (9)$$

with $g_k \in N(0, 2\sigma^2 A_k^2)$. Next, as a sum of Gaussian random variables remains Gaussian distributed, the following holds:

$$\sum_{k=1}^K S_k^0 S_k^{*} \approx A^2 e^{i \frac{v_{enc}}{v_{enc}} v_x} + h^r + i h^i, \quad (10)$$

with $h \in N(0, 2\sigma^2 A^2)$ and $A = A(\mathbf{x})$ as defined in Eq. (4). Finally, the probability distribution after the argument operation in Eq. (8) is given in Eq. (5). Specifically, by applying Eq. (5) to the complex image in Eq. (10), the following key result is obtained:

$$\tilde{v}_x \in N \left(v_x, \frac{v_{enc}^2}{\pi^2} \frac{2\sigma^2}{A^2} \right). \quad (11)$$

Here the unwrapped Gaussian distribution is used as it is standard to correct phase wraps that occur when there are velocities larger than v_{enc} parameter in a pre-processing step using a phase-unwrapping algorithm (Jenkinson, 2003; Salfity et al., 2006).

Expressions analogous to Eq. (11) are valid for the \tilde{v}_y and \tilde{v}_z velocity components too. As each velocity component is Gaussian distributed, the joint distribution of the 3D flow vector $\tilde{\mathbf{v}} = [\tilde{v}_x, \tilde{v}_y, \tilde{v}_z]^T$ is multivariate Gaussian $\tilde{\mathbf{v}} \in N(\mathbf{v}, \Sigma)$. Furthermore, as the baseline images S_k^0 , $k = 1 \dots K$ are involved in the computation of all three velocity components \tilde{v}_x , \tilde{v}_y , and \tilde{v}_z , the covariance matrix Σ will not be diagonal. For example, with derivations similar to the ones above, the covariance between \tilde{v}_x and \tilde{v}_y can be found to be

$$\text{Cov}(\tilde{v}_x, \tilde{v}_y) = \frac{v_{enc}^2}{\pi^2} \frac{\sigma^2}{A^2}. \quad (12)$$

Thus, the full covariance matrix becomes

$$\Sigma = \frac{v_{enc}^2}{\pi^2} \frac{\sigma^2}{A^2} \begin{pmatrix} 2 & 1 & 1 \\ 1 & 2 & 1 \\ 1 & 1 & 2 \end{pmatrix}. \quad (13)$$

It can be noted here that the major difference when a different encoding scheme than the one in Eq. (6) is used, is that the covariance matrix is different. To summarize, the measured flow velocity vector in each voxel may be seen as drawn from a multivariate Gaussian distribution with mean \mathbf{v} , i.e., the true velocity, and covariance matrix as given by Eq. (13). To fully specify the covariance matrix, estimates of the unknown parameters A and σ^2 are required, which is the topic of the next section.

2.3. Parameter estimation

Many methods for estimating the noise variance σ^2 and signal magnitude A_k from magnitude MRI images $|S_k|$ have been proposed in the literature, most of which target the low-SNR case in which the Gaussian approximation of the Rician distribution is no longer valid. For example, in Gudbjartsson and Patz (1995), Henkelman (1985), different correction factors are suggested to obtain the underlying magnitude A_k directly from $|S_k|$. An iterative maximum likelihood estimation approach that accounts for the Rician nature of magnitude MRI images is presented in Sijbers and den Dekker (2004) and an alternative fixed-point algorithm is presented in Koay and Basser (2006). In Constantinides et al. (1997), noise in phased-array acquisitions is considered and estimation based on moment-matching for up to four coils is presented. These methods all have in common that a region with homogenous image intensity must be found, e.g., an artifact-free region in the air where it can be assumed that $A_k = 0$.

Instead, here we propose to utilize the fact that four separate magnitude images of the same object are available in PC MRI flow imaging, i.e., $I^0(\mathbf{x})$, $I^x(\mathbf{x})$, $I^y(\mathbf{x})$, and $I^z(\mathbf{x})$, reconstructed with the sum-of-squares method in Eq. (3). As the noise in the high-SNR voxels within the body have a Gaussian distribution $N(A(\mathbf{x}), \sigma^2)$ (Eq. (4)), the well-known formulas for estimating the mean and variance of Gaussian variables can be applied voxelwise. In appendix A, it is shown that the estimators below comply with the maximum likelihood estimation principle. Let Ω denote the set of all high-SNR voxels in low-flow areas in $I^0(\mathbf{x})$, $I^x(\mathbf{x})$, $I^y(\mathbf{x})$, and $I^z(\mathbf{x})$. These voxels are straightforwardly identified using a threshold operation as they correspond to voxels with high image intensity and low blood flow, i.e., non-air voxels outside major vessels. The reason for excluding high-flow voxels is that they may exhibit flow-related artifacts in the magnitude image. For the voxels in Ω , the Gaussian approximation in Eq. (4) apply and a voxelwise estimator of the signal strength $A(\mathbf{x})$ is obtained as the mean

$$\tilde{A}(\mathbf{x}) = \frac{1}{4} [I^0(\mathbf{x}) + I^x(\mathbf{x}) + I^y(\mathbf{x}) + I^z(\mathbf{x})]. \quad (14)$$

According to Eq. (4), the noise variance σ^2 is equal for all voxels in Ω so that a variance estimate can first be calculated for each voxel separately, and a final estimate then obtained by averaging across all voxels in Ω as follows:

$$\tilde{\sigma}^2 = \frac{1}{(4-1)|\Omega|} \sum_{\mathbf{x}_i \in \Omega} \underbrace{\sum_{k=\{0,x,y,z\}} (I^k(\mathbf{x}_i) - \tilde{A}(\mathbf{x}_i))^2}_{\text{Variance estimate per voxel}}. \quad (15)$$

In this expression, $|\Omega|$ denotes the number of voxels with high-SNR. With $\tilde{A}(\mathbf{x})$ and $\tilde{\sigma}^2$, the covariance matrix for the flow vector in Eq. (13) is fully known. It should be stressed that the above method does not require any user interaction or an image region with homogenous image intensity.

3. Probabilistic flow tracking and uncertainty mapping

In the previous section, the local uncertainty in the measured flow velocity vectors was investigated, and it was shown that the uncertainty can be characterized with a multivariate Gaussian distribution. In this section it is shown how the local uncertainty is propagated to an uncertainty in pathlines and particle traces visualizing the blood flow.

3.1. Probabilistic pathlines and particle traces

The trajectory tracked by a conventional pathline or particle trace in a vector field can be described by train of spatio-temporal 4D vectors $\{\mathbf{s}_0, \mathbf{s}_1, \dots, \mathbf{s}_{n-1}\}$ starting in a spatio-temporal seed point $\mathbf{x}_0 \in \mathbb{R}^4$, see Fig. 2. Each step \mathbf{s}_k is a function of the current trajectory position \mathbf{x}_k , the flow vector field \mathbb{V} , and a temporal step length parameter Δt that controls the length of the step:

$$\mathbf{s}_k = \mathbf{f}(\mathbf{x}_k, \mathbb{V}, \Delta t). \quad (16)$$

An Euler scheme takes a step in the local flow direction $\mathbf{f}(\mathbf{x}_k, \mathbb{V}, \Delta t) \sim \Delta t \mathbb{V}(\mathbf{x}_k)$, but more accurate multistage schemes such as Heun's method or 4th-order Runge–Kutta are generally used in practice to obtain more accurate trajectories (Darmofal and Haines, 1996).

The position of the trajectory after k steps is

$$\mathbf{x}_k = \mathbf{x}_0 + \sum_{j=0}^{k-1} \mathbf{s}_j. \quad (17)$$

The vectors \mathbf{s}_k are traditionally treated as deterministic variables, not considering that the vector field \mathbb{V} is reconstructed from PC MRI images which are contaminated with random noise. If now the vectors in \mathbb{V} instead are treated as random variables as in Section 2.2, the vectors \mathbf{s}_k and the positions \mathbf{x}_k become random variables as well. The key question addressed in this work is the form of the statistical distribution of the point \mathbf{x}_k ,

$$p(\mathbf{x}_k) = p(\mathbf{s}_0, \dots, \mathbf{s}_{k-1}), \quad (18)$$

under the influence of noise in \mathbb{V} . This distribution describes the probability of all possible paths a virtual particle may take from the seed point \mathbf{x}_0 . A theoretical derivation of $p(\mathbf{x}_k)$ is intractable due to the high dimensionality of the distribution as well as the recursive nature of the trajectory, i.e., the vector \mathbf{s}_k depends on all previous vectors $\mathbf{s}_{k-1}, \dots, \mathbf{s}_0$, which is clearly seen by combining Eqs. 16 and 17.

An alternative approach to investigating an intractable probability distribution is to draw random samples from it using computational Monte Carlo methods. In this work, a random sample from $p(\mathbf{x}_k) = p(\mathbf{s}_0, \dots, \mathbf{s}_{n-1})$ is referred to as a *probabilistic pathline* or a *probabilistic particle trace*. A key observation is that Eq. (18) can be factorized into conditionally independent distributions:

$$p(\mathbf{s}_0, \dots, \mathbf{s}_{k-1}) = \prod_{j=0}^{k-1} p(\mathbf{s}_j | \mathbf{x}_j), \quad (19)$$

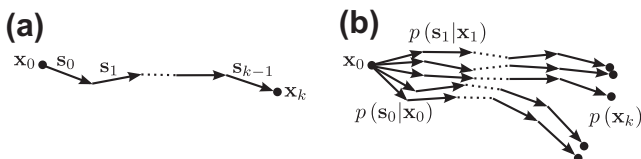


Fig. 2. (a) A vector train describing a conventional pathline or particle trace. (b) Probabilistic pathlines or particle traces are generated using a sequential Monte Carlo method and represent random samples of the distribution of the point $p(\mathbf{x}_k)$.

where each $p(\mathbf{s}_j | \mathbf{x}_j)$ describes the uncertainty in the measured flow vector at the spatio-temporal point \mathbf{x}_j . Note that $p(\mathbf{s}_j | \mathbf{x}_j)$ is 3-dimensional because the image noise affects only the spatial dimensions and not the temporal dimension of \mathbf{s}_j . Random samples from distributions with a factorized form, such as Eq. (19), can be generated using so-called sequential Monte Carlo sampling (Doucet et al., 2001). In this sampling approach, a probabilistic pathline or particle trace is generated iteratively by first drawing a sample $\tilde{\mathbf{s}}_0$ from $p(\mathbf{s}_0 | \mathbf{x}_0)$, which gives $\tilde{\mathbf{x}}_1 = \mathbf{x}_0 + \tilde{\mathbf{s}}_0$. Next, given $\tilde{\mathbf{x}}_1$, a sample $\tilde{\mathbf{s}}_1$ can be drawn from $p(\mathbf{s}_1 | \tilde{\mathbf{x}}_1)$, which gives $\tilde{\mathbf{x}}_2$, and so on, see Fig. 2b. Note that thousands of probabilistic pathlines or particle traces can be generated in this way.

It remains to find the 3D probability distribution of the step direction $p(\mathbf{s}_j | \mathbf{x}_j)$ in Eq. (19). In Section 2.2, it was shown that the measured flow directions follow a multivariate 3D Gaussian distribution $\mathbb{V}(\mathbf{x}_k) \in N(\mathbf{v}_k, \Sigma)$ around a true velocity \mathbf{v}_k and a covariance matrix Σ . Therefore, noting that the step length Δt acts as a scaling factor of $\mathbb{V}(\mathbf{x}_k)$ to obtain a tracking step in Eq. (16), $p(\mathbf{s}_j | \mathbf{x}_j)$ is also modeled to have a Gaussian form:

$$p(\mathbf{s}_j | \mathbf{x}_j) \in N[\mathbf{f}(\mathbf{x}_j, \mathbb{V}; \Delta t), \Delta t^2 \Sigma]. \quad (20)$$

Expressed in words, the random vector \mathbf{s}_j has as mean the deterministic vector described by Eq. (16) that is obtained using a regular tracing algorithm, e.g., an Euler, Heun or Runge–Kutta scheme. The spatial components of this vector are perturbed with the covariance matrix Σ scaled by the step length Δt . In appendix B, it is shown how to generate random samples from a multivariate Gaussian distribution with covariance matrix Σ .

Finally, a remark on the choice of step length Δt : When $\Delta t \rightarrow 0$, the variance of $p(\mathbf{s}_j | \mathbf{x}_j)$ in Eq. (20) also approaches zero and the probabilistic particle trace will approach the conventional deterministic particle trace. Note that the uncertainty is estimated on the voxel scale; if another spatial resolution of the PC MRI images is chosen, the noise variance would also change. Therefore, the step length Δt should be set so that the spatial length of each step is of the same order as the grid resolution of \mathbb{V} , i.e., the voxel size of the PC MRI images.

3.2. Flow uncertainty map

The probabilistic particle traces described in the previous section are random samples from the probability distribution over all possible trajectories in the 4D spatio-temporal space, where the randomness stems from the PC MRI image noise. To visualize this distribution, a histogram $\Psi(\mathbf{x})$ based on the samples can be calculated. A bin of the histogram may be set to a voxel in the PC MRI images, but a finer grid can also be used. Let $\mu(\mathbf{x}_k)$ be the number of occasions a probabilistic particle trace passes through the volume occupied by voxel \mathbf{x}_k . A normalized histogram is then calculated as

$$\Psi(\mathbf{x}_k) = \frac{\mu(\mathbf{x}_k)}{N}. \quad (21)$$

A large number $N > 5000$ of probabilistic particle traces are required for an accurate histogram estimate. The resulting histogram is in this application referred to as a flow uncertainty map, although it depicts certainty rather than uncertainty. Certainty and uncertainty are directly related through an inverse relationship, so that these terms can be used interchangeably.

4. Data

To demonstrate the methods presented in the previous sections, four 4D PC MRI data sets are used. These data sets were chosen because they exhibit a variety of geometries and flow patterns. Three



Fig. 3. SNR map of one slice in a PC MRI data set. The SNR within the body and within the aorta is around 10 or higher.

of the data sets cover the aorta and were acquired as described in Markl et al. (2007): one data set from a healthy volunteer, one from a patient with an aortic aneurysm, and one from a patient with a retrograde flow pattern, i.e., a back-flow of blood. The fourth data set covers the bifurcation of the carotid arteries and was acquired as described in Harloff et al. (2009). The vessel geometries are shown in Fig. 6. The data sets were acquired with the following sequence parameters: TE = 2.6–3.7 ms, TR = 5.1–5.6 ms, flip angle 15, $v_{enc} = 1.5$ m/s, $K = 12$ coils and a temporal resolution of 41–45 ms. The aorta data sets have a matrix size of $140 \times 190 \times 25$ voxels and a spatial resolution of $1.7 \times 1.7 \times 3$ mm. The carotid data set has a matrix size of $208 \times 256 \times 36$ voxels and spatial resolution of $0.86 \times 0.86 \times 1.4$ mm. All data sets have between 14 and 20 temporal frames covering one heart beat.

5. Results

The probabilistic particle tracing and uncertainty map generation were implemented in C++ and integrated as modules in the

software platform MeVisLab (www.mevislab.de). In the sections below, the high SNR assumption and the derived probability distribution of the velocity components are first verified using both simulated and real data. The real PC MRI data sets are then used to illustrate the probabilistic particle traces and flow uncertainty maps.

5.1. Signal-to-noise estimation

Throughout Section 2 it was assumed that the PC MRI images have sufficient SNR for making Gaussian noise approximations. This assumption is verified here by estimating $A(\mathbf{x})$ and σ^2 in Eq. (4) according to the procedure outlined in Section 2.3. The result is presented as the estimated $\text{SNR} = A(\mathbf{x})/\sigma$, which is the relevant quantity in Eqs. 11 and 13, e.g., for making a Gaussian approximation of the Rician distribution. An image of the estimated SNR values for one PC MRI image slice and time point is shown in Fig. 3. The SNR in the aorta is around 10, which is high enough to warrant Gaussian noise approximations. Furthermore, this value leads to a standard deviation induced by noise of $\frac{v_{enc}}{\pi} \frac{\sqrt{2}\sigma}{A} = 68$ mm/s of each velocity component in Eq. (11), which can be compared with normal flow velocities ranging between zero in the mid RR interval and 1200 mm/s and 800 mm/s in the aorta and in the carotid arteries respectively at peak systolic flow.

5.2. Velocity distribution

In this simulation study, the accuracy of the theoretically derived Gaussian distribution in Eq. (11) of the flow velocity components is investigated. To this end, synthetic images that mimic real PC MRI images were first generated according to Eq. (6). A circular disk was embedded in noise, see Fig. 4a. The size of the image was 256×256 pixels and the noise variance and the intensity magnitude of the disk were adjusted to obtain an SNR of $A(\mathbf{x})/\sigma = 10$. Note that the shape and size of the simulated flow region have no bearing on the result as the velocities are estimated voxel-wise. To further mimic the real data situation described in Section 4, 12 coils with different spatial sensitivities evenly distributed over the image were simulated. For each coil k , four PC images S_k^0 , S_k^x , S_k^y , and S_k^z (cf. Eq. (6)) were simulated with different noise realizations. The complex phase of the images was modified to simulate the same flow vector $\mathbf{v} = [-0.5, 0, 0.5]$ m/s in all pixels within the disk. A $v_{enc} = 1.5$ m/s was used. Based on the simulated images, the flow velocities were estimated according to Eq. (8), see Fig. 4b for the estimated \tilde{v}_x component. A histogram for each estimated velocity \tilde{v}_x , \tilde{v}_y , and \tilde{v}_z over all voxels is plotted in Fig. 5 together with the theoretically derived Gaussian distributions in Eq. (11). The estimated velocities are centered around the true values $-0.5, 0,$

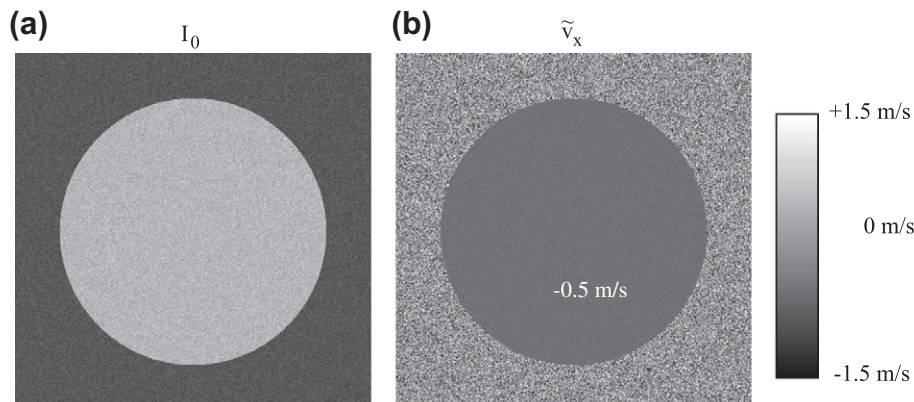


Fig. 4. (a) Magnitude image $I(\mathbf{x})$ (cf. Eq. (3)) showing a simulated disk with a flow $\mathbf{v} = [-0.5, 0, 0.5]$ m/s. (b) The estimated velocity \tilde{v}_x in the x -direction. The true velocity is -0.5 m/s.

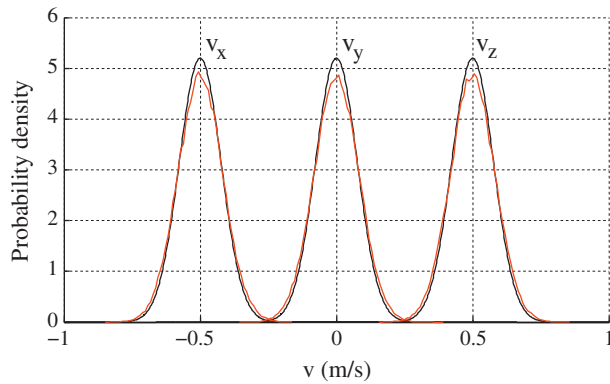


Fig. 5. The red distributions show histograms of the estimated velocities in the disk region in Fig. 4. The theoretically derived Gaussian distributions of the velocity components in Eq. 11 are shown in black. (For interpretation of the references to color in this figure legend, the reader is referred to the web version of this article.)

and 0.5, and the simulated distributions follow the Gaussian distributions well. This empirical investigation supports the derivations in Section 2 and the Gaussian nature of the estimated flow vectors.

5.3. Flow uncertainty mapping

This section shows real data examples of probabilistic pathlines, particle traces and flow uncertainty maps. The four PC MRI data sets are visualized in Fig. 6. The probabilistic pathlines and particle traces were generated using a 4th-order Runge–Kutta scheme with a step length equal to the voxel size, as discussed in Section 3.1. The trajectories were terminated if they left a predefined segmentation mask of the vessel, or when the length exceeded a threshold. The length threshold can be set in both in terms of the maximum number of steps, e.g., 200, or in seconds, e.g. 0.5 s.

The top panel shows traditional pathlines generated using a 4th-order Runge–Kutta scheme. The middle panel in Fig. 6 shows probabilistic pathlines and the bottom panel the corresponding flow uncertainty maps. The normal aorta data set is shown in Fig. 6a, with a pathline started at the beginning of the heart beat visualizing the estimated trajectory a mass-less particles takes in the 4D flow vector field. Note that this visualization does not convey any kind of uncertainty in the trajectory. By contrast, the probabilistic pathlines show that there is actually an uncertainty as to in which supra-aortic vessel the flow exits. The probabilistic pathlines were generated according to Section 3.1 with the variance parameter settings estimated in Section 5.1. It should be stressed that all probabilistic pathlines originate from the same point. The

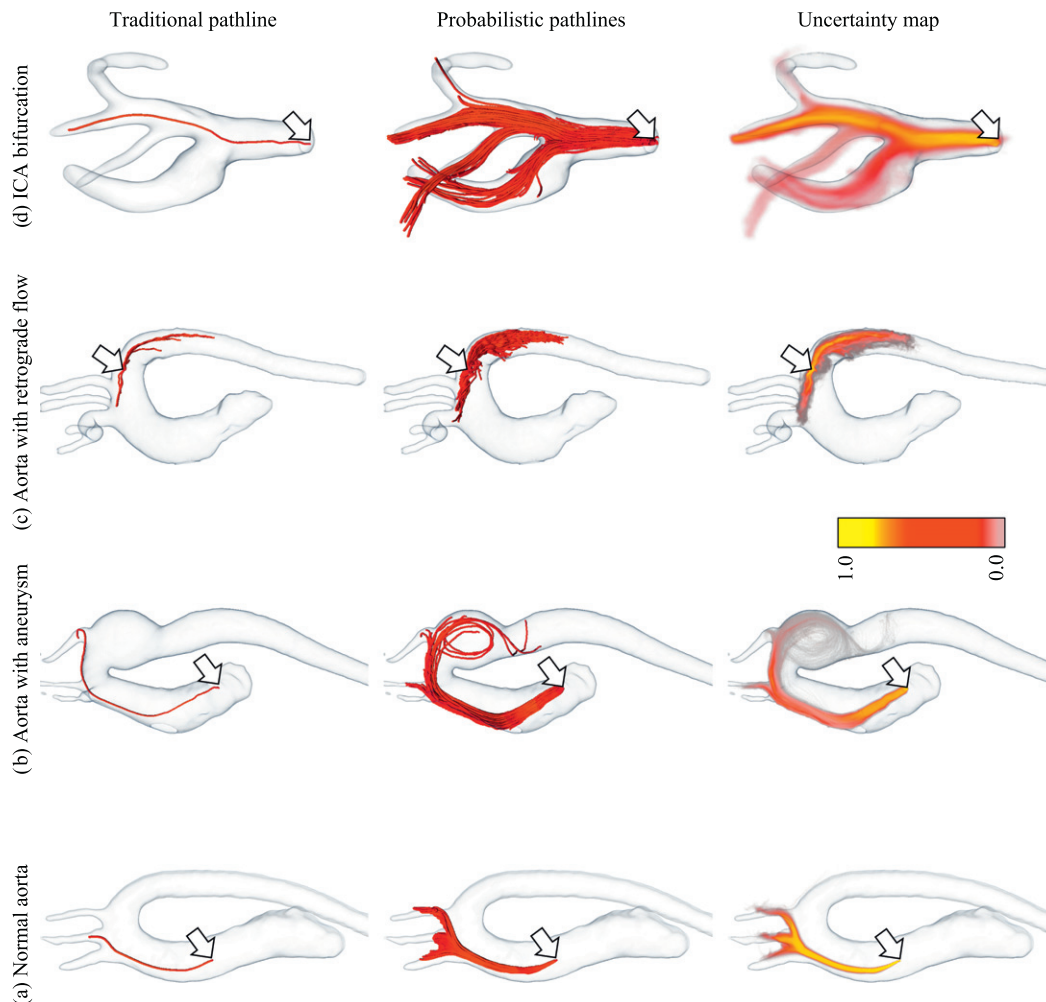


Fig. 6. Real data examples of flow in the aorta and in the carotid bifurcation. For each example, the traditional pathline starting at the point marked by the arrow is shown, as well as 200 probabilistic pathlines initiated at the same point and uncertainty maps based on 40,000 probabilistic pathlines. (a) The aorta of a healthy person. The probabilistic pathlines show the uncertainty regarding which vessel branch the flow ends in. (b) An aorta with an aneurysm. (c) A patient with retrograde flow, i.e., a back-flow. The uncertainty map shows how blood is flowing back, reaching the carotid and subclavian arteries. (d) Flow in a carotid bifurcation.

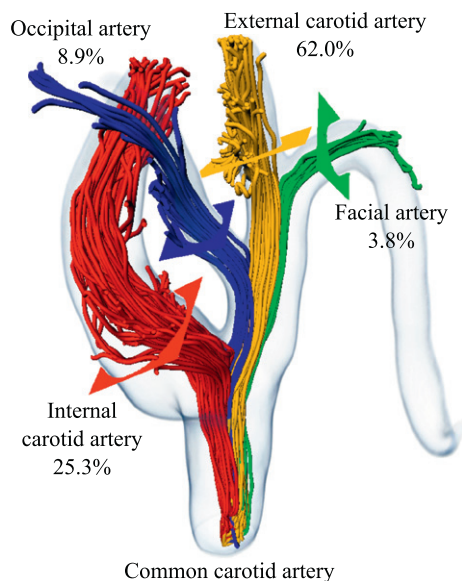


Fig. 7. Clustering and quantification of probabilistic pathlines starting in the common carotid artery. The numbers show the fraction of pathlines that passes each colored plane defining an artery branch: external carotid artery (yellow) 62.0%, internal carotid artery (red) 25.3%, occipital artery (blue) 8.9%, facial artery (green) 3.8%. (For interpretation of the references to color in this figure legend, the reader is referred to the web version of this article.)

uncertainty is further quantified by the flow uncertainty map in the bottom panel. In Fig. 6b, an aortic aneurysm is shown, in which a vortex flow pattern is formed. In Fig. 6c, the data set with retrograde back-flow in the aorta is shown. Pathlines were seeded at multiple time points to show the back-flow of blood during the heart cycle. The probabilistic pathlines and the uncertainty map indicate that the back-flow reaches the supra-aortic vessels, and that a ruptured plaque therefore may be transported back with the flow and reach the brain, where it can cause a stroke. Finally, Fig. 6d shows the flow and uncertainty through the carotid artery bifurcation. Another way of quantifying the uncertainty is shown

in Fig. 7, where the probabilistic pathlines have been colored according to which of the predefined image planes it passes through. It shows that the pathline originating at this particular emitter point is most likely to travel along the External carotid artery (yellow plane, 62.0%), followed by the Internal carotid artery (red plane, 25.3%).

The PC MRI data sets are 4-dimensional and the flow can therefore be visualized as an animation using time-resolved particle traces. Equivalent probabilistic particle traces can be generated as explained in Section 3.1, and the associated uncertainty map can also be visualized as a 4D animation. This is illustrated in Fig. 8 for the normal aorta data set and the carotid bifurcation. Movies are available as [Supplementary material](#).

The computation of probabilistic particle traces is fast as it only involves linear interpolation of vectors when tracing the paths (using the Euler, Heun or Runge–Kutta schemes) and generating Gaussian random variables for the Monte Carlo sampling. The computations are also trivially parallelized as the probabilistic particle traces can be sampled independently of each other. The 40,000 probabilistic pathlines underlying the uncertainty maps in Figs. 6 and 8 are therefore generated in a few seconds on a modern PC.

6. Discussion

The presented work is, to the best of our knowledge, the first to address uncertainty in 4D flow analysis based on PC MRI data. The uncertainty analysis can be seen as a perturbation analysis which investigates how sensitive the flow trajectories are to variations of the noise. The result is a flow uncertainty map that is based on the concept of probabilistic pathlines and particle traces. In contrast to conventional flow visualization techniques, the uncertainty map conveys directly the uncertainty due to measurement noise. It is important to stress that the uncertainty map is not showing the distribution of flow one would, for example, see if a concentration of dye was released in a flow, but rather the probability distribution of the trajectory a mass-less particle takes with different measurement noise realizations. There are other types of uncertainty that can be modeled and included as well, in particular the intra-voxel distribution of flow. The standard deviation of the flow

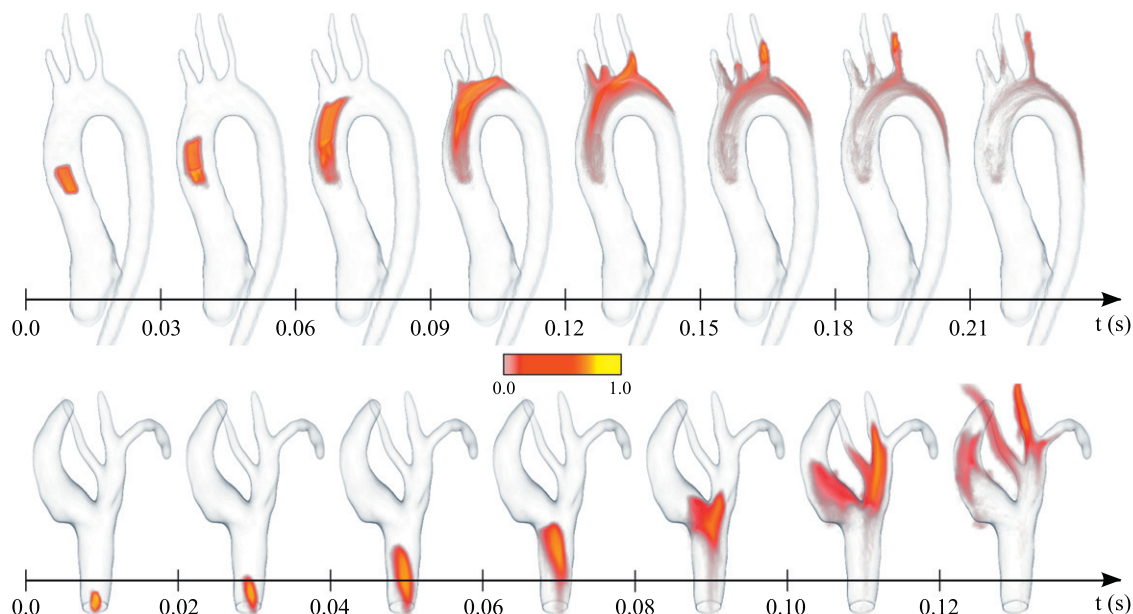


Fig. 8. Time-resolved 4D flow uncertainty maps showing the probability distribution of particle traces over one heart beat in the normal aorta (upper panel) and the carotid bifurcation (lower panel) data sets.

direction distribution within a voxel can be measured (Dyverfeldt et al., 2006), and this information can potentially be used as an additional variance component. More research on modeling turbulent flow from an uncertainty perspective must be carried out to this end, but the ensuing uncertainty map could then be interpreted as a flow distribution. Other sources of uncertainty include image artefacts and partial volume effects at the vessel borders. An example of the partial volume effect can be seen in Fig. 6a, where the pathlines terminate prematurely after the bifurcation due to corrupted velocity measurements in the smaller vessels.

A weakness of the presented method is that the best estimate we have of the true velocity v is the single measurement \tilde{v} in Eq. (11). This means that the probabilistic particle traces in Eq. (20) are based on a noisy estimate, which may bias the flow uncertainty map. Note, however, that the spread of the uncertainty map will still be correct. Nevertheless, this possible bias has implications for quantifications based on the uncertainty analysis that must be further investigated. For example, possible applications include quantifying the blood mixing ratio where two blood vessels meet, or calculating the probabilities for different stroke embolization pathways. The next step in this direction should be to validate quantification results using physical flow phantoms.

Finally, another avenue of future work is to extend and adapt the statistical modeling in Section 2 to other MRI acquisition techniques for flow measurement. The PC MRI technique is undergoing strong development, and from an acquisition perspective, there are different alternatives to choose from. For example, the PC MRI acquisition time is currently relatively long, about 20 to 30 minutes, and it is of clinical interest to reduce this time using parallel imaging (Dietrich et al., 2007). In this work, parallel coils were considered to obtain maximum SNR, but one can also trade SNR for a shorter acquisition time. A side effect of this is a spatially varying noise variance due to the conditioning of the image reconstruction problem, which complicates the noise estimation process described in Section 2.3. Understanding the noise in parallel MRI is currently an active research question (Koay and Basser, 2006; Aja-Fernandez et al., 2009; Aja-Fernandez et al., 2011). Another acquisition option is the flow encoding scheme, which was discussed in Section 2.2. One must also pay attention to artifacts associated with different acquisition techniques that may violate the assumptions in the statistical modeling, e.g., that the mean and variance of the image magnitude do not vary in intensity depending on the velocity encoding. This problem may arise with some acquisition sequences (O'Brien et al., 2008), but generally not with the one used in this work (Bernstein et al., 1992). Nevertheless, it should be stressed that alternative approaches to estimating the noise variance are available as discussed in Section 2.3. One may also use robust estimation alternatives based on the median that are more resilient to outliers and artefacts, instead of the regular mean and variance estimates. Yet another alternative is to acquire noise images in addition to the PC MRI images. For example, using a zero flip angle but otherwise identical scan parameters would provide a spatially resolved noise map which could be used for a detailed analysis of global and regional noise characteristics.

7. Conclusions

Probabilistic flow tracking and uncertainty in 4D PC MRI flow measurements have been addressed in this work. The local statistical properties of the measured flow vectors were derived and a novel estimation approach for finding the noise variance and SNR proposed. The concept of probabilistic pathlines and particle traces, which are generated using sequential Monte Carlo sampling, was introduced as a means to propagate the local measurement uncertainty to a global flow uncertainty map. Each

probabilistic pathline is a sample of the distribution of all possible flow trajectories under the influence of random measurement noise. The theoretical derivations were validated using simulated data and the visualization of flow uncertainty maps was demonstrated using various PC MRI data sets with different pathologies.

Appendix A

In this section, it is shown that the variance estimation in Eq. (15) conforms with the maximum likelihood (ML) estimation principle. Let x_k^m , $m = 1 \dots M$, be observations drawn from a Gaussian distribution $N(\mu_k, \sigma^2)$, and assume that we have M such observations from each of a collection of K different Gaussian distributions with the same variance σ^2 but with different means μ_k , $k = 1 \dots K$. This is the situation in Section 2.3, where M equals 4 and K the number of voxels. The likelihood function is

$$L(\mu_1, \dots, \mu_K, \sigma^2) = \prod_{k=1}^K \prod_{m=1}^M \frac{1}{\sqrt{2\pi\sigma^2}} e^{-\frac{(x_k^m - \mu_k)^2}{2\sigma^2}}. \quad (22)$$

Maximizing Eq. (22) yields the same solution as maximizing the logarithm

$$\begin{aligned} \ln L(\mu_1, \dots, \mu_K, \sigma^2) = & -\frac{K+M}{2} \ln(2\pi\sigma^2) - \frac{1}{2\sigma^2} \sum_{k=1}^K \\ & \times \sum_{m=1}^M (x_k^m - \mu_k)^2. \end{aligned} \quad (23)$$

Setting the partial derivative of Eq. (23) with respect to μ_k to zero yields the familiar estimator of the mean $\tilde{\mu}_k = \frac{1}{M} \sum_{m=1}^M x_k^m$, which corresponds to Eq. (14). Setting the partial derivative of Eq. (23) with respect to σ^2 to zero, and replacing μ_k with $\tilde{\mu}_k$ yields

$$\tilde{\sigma}^2 = \frac{1}{KM} \sum_{k=1}^K \sum_{m=1}^M (x_k^m - \tilde{\mu}_k)^2. \quad (24)$$

This is the ML estimator used in Eq. (15), except that Eq. (15) is normalized with $M - 1$ instead of with M to correct for the well known bias in the ML estimator.

Appendix B

In this section it is briefly explained how to generate a multivariate Gaussian random variable \mathbf{y} with a certain covariance matrix Σ (cf. Eq. (13)). First, the Cholesky decomposition $\Sigma = \mathbf{K}^T \mathbf{K}$ is calculated, giving the upper-triangular matrix \mathbf{K} . Next, a vector \mathbf{x} of independent $N(0,1)$ random variables is generated. \mathbf{y} is now found as

$$\mathbf{y} = \mathbf{K}^T \mathbf{x}. \quad (25)$$

One can verify that the covariance equals $\text{Cov}(\mathbf{y}) = \text{Cov}(\mathbf{K}^T \mathbf{x}) = \mathbf{K}^T \text{Cov}(\mathbf{x}) \mathbf{K} = \mathbf{K}^T \mathbf{K} = \Sigma$.

Appendix C. Supplementary material

Supplementary data associated with this article can be found, in the online version, at doi:10.1016/j.media.2011.06.002.

References

- Aja-Fernandez, S., Tristan-Vega, A., Alberola-Lopez, C., 2009. Noise estimation in single- and multiple-coil magnetic resonance data based on statistical models. *Magn. Reson. Imag.* 27, 1397–1409.
- Aja-Fernandez, S., Tristan-Vega, A., Hoge, W., 2011. Statistical noise analysis in GRAPPA using a parametrized noncentral Chi approximation model. *Magn. Reson. Med.* 65, 1195–1206.
- Andersen, A., 1996. On the Rician distribution of noisy MRI data. *Magn. Reson. Med.* 36, 331–332.

- Andersen, A.H., Kirsch, J.E., 1996. Analysis of noise in phase contrast MR imaging. *Med. Phys.* 23, 857–869.
- Behrens, T., Woolrich, M., Jenkinson, M., Johansen-Berg, H., Nunes, R., Clare, S., Matthews, P., Brady, J., Smith, S., 2003. Characterization and propagation of uncertainty in diffusion-weighted MR imaging. *Magn. Reson. Med.* 50, 1077–1088.
- Bernstein, M., Shimkawa, A., Pelc, N., 1992. Minimizing TE in moment-nulled or flow-encoded two- and three-dimensional gradient-echo imaging. *J. Magn. Reson. Imag.* 2, 583–588.
- Björnemo, M., Brun, A., Kikinis, R., Westin, C.F., 2002. Regularized stochastic white matter tractography using diffusion tensor MRI, in: *Proceedings of the 5th International Conference on Medical Image Computing and Computer Assisted Intervention (MICCAI'02)*, pp. 435–442.
- Constantinides, C., Atalar, E., McVeigh, E., 1997. Signal-to-noise measurements in magnitude images from NMR phased arrays. *Magn. Reson. Med.* 38, 852–857.
- Conturo, T., Robinson, B., 1992. Analysis of encoding efficiency in MR imaging of velocity magnitude and direction. *Magn. Reson. Med.* 25, 233–247.
- Conturo, T., Smith, G., 1990. Signal-to-noise in phase angle reconstruction: dynamic range extension using phase reference offsets. *Magn. Reson. Med.* 15, 420–437.
- Darmofal, D., Haimes, R., 1996. An analysis of 3D particle path integration algorithms. *J. Comput. Phys.* 123, 182–195.
- Dietrich, O., Raya, J., Reeder, S., Reiser, M., Schoenberg, S., 2007. Measurement of signal-to-noise ratios in MR images: influence of multichannel coils, parallel imaging, and reconstruction filters. *J. Magn. Reson. Imag.* 26, 375–385.
- Doucet, A., de Freitas, N., Gordon, N. (Eds.), 2001. *Sequential Monte Carlo Methods in Practice*. Springer-Verlag, New York.
- Dyverfeldt, P., Sigfridsson, A., Kvitting, J., Ebbens, T., 2006. Quantification of intravoxel velocity standard deviation and turbulence intensity by generalizing phase-contrast MRI. *Magn. Reson. Med.* 56, 850–858.
- Firmin, D., Nayler, G., Klipstein, R., Underwood, S., RS, R.R., Longmore, D., 1987. In vivo validation of MR velocity imaging. *J. Comput. Assist. Tomogr.* 11, 751–756.
- Friman, O., Farneback, G., Westin, C.F., 2006. A Bayesian approach for stochastic white matter tractography. *IEEE Trans. Med. Imag.* 25, 965–978.
- Friman, O., Hennemuth, A., Harloff, A., Bock, J., Markl, M., Peitgen, H.O., 2010. Probabilistic 4D blood flow mapping, in: *Proceedings of the 13th International Conference on Medical Image Computing and Computer Assisted Intervention (MICCAI'10)*, pp. 416–423.
- Gudbjartsson, H., Patz, S., 1995. The Rician distribution of noisy MRI data. *Magn. Reson. Med.* 34, 910–914.
- Hagmann, P., Thiran, J., Jonasson, L., Vandergheynst, P., Clarke, S., Maeder, P., Meuli, R., 2003. DTI mapping of human brain connectivity: Statistical fibre tracking and virtual dissection. *NeuroImage* 19, 545–554.
- Harloff, A., Albrecht, F., Spreer, J., Stalder, A., Bock, J., Frydrychowicz, A., Schollhorn, J., Hetzel, A., Schumacher, M., Hennig, J., Markl, M., 2009. 3D blood flow characteristics in the carotid artery bifurcation assessed by flow-sensitive 4D MRI at 3T. *Magn. Reson. Med.* 61, 65–74.
- Henkelman, R., 1985. Measurement of signal intensities in the presence of noise in MR images. *Med. Phys.* 12, 232–233.
- Jenkinson, M., 2003. Fast, automated, N-dimensional phase-unwrapping algorithm. *Magn. Reson. Med.* 49, 193–197.
- Jones, D., Pierpaoli, C., 2005. Confidence mapping in diffusion tensor magnetic resonance imaging tractography using a bootstrap approach. *Magn. Reson. Med.* 53, 1143–1149.
- Koay, C.G., Basser, P.J., 2006. Analytically exact correction scheme for signal extraction from noisy magnitude MR signals. *J. Magn. Reson.* 179, 317–322.
- Macovski, A., 1996. Noise in MRI. *Magn. Reson. Med.* 36, 494–497.
- Markl, M., Harloff, A., Bley, T., Zaitsev, M., Jung, B., Weigang, E., Langer, M., Hennig, J., Frydrychowicz, A., 2007. Time-resolved 3D MR velocity mapping at 3T: improved navigator-gated assessment of vascular anatomy and blood flow. *J. Magn. Reson. Imag.* 25, 824–831.
- Napel, S., Lee, D., Frayne, R., Rutt, B., 1992. Visualizing three-dimensional flow with simulated streamlines and three-dimensional phase-contrast MR imaging. *J. Magn. Reson. Imag.* 2, 143–153.
- Nayler, G., Firmin, D., Longmore, D., 1986. Blood flow imaging by cine magnetic resonance. *J. Comput. Assist. Tomogr.* 10, 715–722.
- O'Brien, K., Cowan, B., Jain, M., Stewart, R., Kerr, A., Young, A., 2008. MRI phase contrast velocity and flow errors in turbulent stenotic jets. *J. Magn. Reson. Imag.* 28, 210–218.
- Parker, G., Alexander, D., 2005. Probabilistic anatomical connectivity using persistent angular structure obtained from diffusion weighted imaging. *Philos. Trans. Roy. Soc. Lond. B: Biol. Sci.* 360, 893–902.
- Parker, G., Haroon, H., Wheeler-Kingshott, C., 2003. A framework for a streamline-based probabilistic index of connectivity (PICO) using a structural interpretation of MRI diffusion measurements. *J. Magn. Reson. Imag.* 18, 242–254.
- Pelc, N., Bernstein, M., Shlmakawa, A., GH, G.G., 1991a. Encoding strategies for three-direction phase-contrast MR imaging of flow. *J. Magn. Reson. Imag.* 1, 405–413.
- Pelc, N., Herfkens, R., Shimakawa, A., Enzmann, D., 1991b. Phase contrast cine magnetic resonance imaging. *Magn. Reson. Quart.* 7, 229–254.
- Pelc, N., Sommer, F., Li, K., Brosnan, T., Herfkens, R., Enzmann, D., 1994. Quantitative magnetic resonance flow imaging. *Magn. Reson. Quart.* 10, 125–147.
- Rice, S., 1944. Mathematical analysis of random noise. *Bell Syst. Tech. J.*, 282–332.
- Roemer, P., Edelstein, W., Hayes, C., Souza, S., Mueller, O., 1990. The NMR phased array. *Magn. Reson. Med.* 16, 192–225.
- Salftly, M.F., Huntley, J.M., Graves, M.J., Marklund, O., Cusack, R., Beauregard, D.A., 2006. Extending the dynamic range of phase contrast magnetic resonance velocity imaging using advanced higher-dimensional phase unwrapping algorithms. *J. Roy. Soc. Interface* 3, 415–427.
- Sijbers, J., den Dekker, A.J., 2004. Maximum likelihood estimation of signal amplitude and noise variance from MR data. *Magn. Reson. Med.* 51, 586–594.
- Thunberg, P., Karlsson, M., Wigström, L., 2005. Comparison of different methods for combining phase-contrast images obtained with multiple coils. *Magn. Reson. Imag.* 23, 795–799.
- Wigström, L., Ebbens, T., Fyrenius, A., Karlsson, M., Engvall, J., Wranne, B., Bolger, A., 1999. Particle trace visualization of intracardiac flow using time-resolved 3D phase contrast MRI. *Magn. Reson. Med.* 41, 793–799.
- Wigström, L., Sjöqvist, L., Wranne, B., 1996. Temporally resolved 3D phase-contrast imaging. *Magn. Reson. Med.* 36, 800–803.